Effect of processing parameters on the relative density of AlSi10Mg processed by laser powder bed fusion

Even Wilberg Hovig[1], Håkon Dehli Holm[1], Knut Sørby[1]

Abstract. In order for a material processed by laser powder bed fusion (LPBF) to achieve the desired mechanical properties, the relative density of the material should be as high as possible. In this study, the effect of various processing parameters of a LPBF process have been investigated in order to increase the relative density of processed AlSi10Mg. The results show that pre-heating the powder and increasing the substrate temperature increases both the relative density and build rate. In addition, a novel method to select the processing parameters, based on the laser penetration depth, has been proposed.

Keywords: Laser Powder Bed Fusion; Additive Manufacturing; AlSi10Mg; Relative Density; Selective Laser Melting; Process Parameter

1 Introduction

Laser powder bed fusion (LPBF) is a process where a component is manufactured layer by layer from a three-dimensional CAD model. The feedstock material is typically a pre-alloyed powder, which is distributed in a thin layer over a substrate of a (usually) similar alloy. The first layer is melted by a laser, before the substrate is moved down by the distance of a layer height, and a new layer of powder is distributed over the preceding layer. The second layer is then melted, before the process repeats itself until a finished geometry is produced. The substrate may, or may not be, heated, and the process takes place in a controlled atmosphere, usually with inert gas to minimize the oxygen content in the build chamber.

LPBF has some specific challenges when compared to traditional manufacturing methods such as casting. The challenges includes, but are not limited to, high cooling rates [1], elongated grain growth [2], and melt pool effects such as spatter [3].

The high cooling rates contributes to residual stresses in LPBF components which tends to be compressive in the centre of the component, and tensile near the edges [4]. This in turn may lead to cracks or distortion in the material. Distortion during LPBF processing can result in incomplete coating in subsequent layers. Another challenge with the high cooling rate is the possibility of forming keyhole pores. A keyhole pore is a result of rapid solidification and incomplete filling of molten material [5]. A keyhole pore is typically irregular in shape, and large in size (Ø > 100 μm). For LPBF of

[1] E. W. Hovig (✉)
Norwegian University of Science and Technology, 7031, Trondheim, Norway
e-mail: even.w.hovig@ntnu.no

AlSi10Mg, the high cooling rate also results in a very fine grain structure, which increases the tensile properties at the cost of ductility [6].

The direction of the thermal gradient is parallel to the build direction, perpendicular to the substrate, which leads to elongated grain growth parallel to the build direction. This leads to a crystallographic texture, which in turn leads to anisotropic mechanical properties [2].

Spatter may refer to either droplet spatter, or powder spatter [7]. Droplet spatter occurs due to the dynamics of the melt pool, and refers to the propulsion of spherical particles out of the melt pool [8]. Powder spatter occurs when powder particles are blown away by the metallic vapour [7]. The particle size of the droplet spatter is up to three times larger than the powder particles, and contains more oxygen than the average component [7]. In addition to the increased oxygen content, the large particles may increase the risk of incomplete powder coating of the next layer, or disturb neighbouring layers, resulting in porosity in the bulk material.

Another cause of porosity in LPBF AlSi10Mg is entrapment of gas, either hydrogen or the processing gas (usually argon) [5]. The powder feedstock may also contain trapped gas pores, which may manifest itself into the processed material.

In order to achieve the desired mechanical properties the relative density of the processed material should be as high as possible [9], and the processing parameters must be selected to reduce the porosity. Several studies have investigated the effect of various processing parameters on the relative density of LPBF materials [5, 9, 10]. The key parameters are listed in Table 1.

Table 1. Key processing parameters for laser powder bed fusion.

Laser parameters	Symbol	Unit
Laser power	P	W
Laser scan velocity	v	mm/s
Hatch spacing	h	µm
Laser focus diameter	d	µm
Build parameters		
Layer thickness	t	µm
Substrate temperature	T_s	°C
Scan strategy	-	-

2 Materials and methods

Two sets of 19 cubes of 10x10x10 mm^3 were produced with different processing parameters in a Concept Laser M2 Cusing powder bed fusion machine. Continuous heating of the substrate was done with a heated platform designed and installed in the LPBF machine by the authors. The AlSi10Mg powder feedstock was supplied by Concept Laser, with the chemical composition as listed in Table 2. Argon was used as processing gas to keep the oxygen content below 0.2% during processing.

Table 2. Chemical composition of the powder feedstock according to the supplier.

Si	Mg	Fe	Mn	Ti	Cu	Zn	C	Al
9.0-11.0	0.2-0.45	<0.55	<0.45	<0.15	<0.1	<0.1	<0.05	bal.

Initial tests prior to this study [11] revealed that Concept Laser's *Island* scan strategy combined with a pre-scan of each layer with a laser power of 50 W yields the best results in terms of relative density. The islands were 5x5 mm^2 with an angular shift of 45° and X- and Y shift of 1 mm. The remaining processing parameters are listed in Table 3.

Table 3. Processing parameters used.

Test number	Laser Power, P	Scan velocity, v	Hatch Spacing, h	Layer thickness, t	Substrate temperature, T_s
	(W)	(mm/s)	(μm)	(μm)	(°C)
1	200	1025	97.5	30	25
2	200	1100	97.5	30	25
3	200	1200	97.5	30	25
4	200	1025	97.5	60	25
5	200	500	105	60	25
6	200	925	97.5	30	200
7	200	1025	97.5	30	200
8	200	1050	97.5	30	200
9	200	1075	97.5	30	200
10	200	1100	97.5	30	200
11	200	1125	97.5	30	200
12	200	1150	97.5	30	200
13	200	1175	97.5	30	200
14	200	1200	97.5	30	200
15	200	1225	97.5	30	200
16	200	1250	97.5	30	200
17	200	1275	97.5	30	200
18	200	1300	97.5	30	200
19	200	1400	97.5	30	200

One set of the cubes was cut in the XY plane (parallel to the substrate) and the other set of cubes in the Z plane (parallel to the build direction). The cut cubes were cast in resin and mechanically ground and polished to a mirror finish. The surfaces were investigated in a Leica MeF4 optical microscope with a Jenoptik Laser Optik system camera of the type ProgRes C10 plus. The high resolution optical images were stitched together using image manipulation software. The relative density of the cubes was found by measuring the porosity by use of ImageJ, and categorized based on size and circularity.

The relative density of the cubes were determined by cutting one set of cubes in the XY plane (parallel to the substrate) and the other set of cubes in the Z plane (parallel to

the build direction). The cut cubes were cast in resin and mechanically ground and polished to a roughness of 0.04 μm. The mirror-finish surfaces were investigated in a Leica MeF4 optical microscope with a Jenoptik Laser Optik system camera of the type ProgRes C10 plus. The high resolution optical images were stitched together using image manipulation software. The porosity was measured using ImageJ, and categorized based on size and circularity.

3 Results and discussion

The relative density, and amount and type of porosity is listed in Table 4. Metallurgical pores are defined to have an area smaller than 3000 μm^2, and a circularity above 0.8 (a circularity of 1 is by definition a perfect circle, and the circularity will approach 0 when the shape becomes more and more elongated). Disrupted oxides are defined to be smaller than 3000 μm^2, but with a circularity lower than 0.8. Large pores have an area greater than 3000 μm^2.

Table 4. Average porosity and relative density for the XY and Z planes.

Test number	Metallurgical pores	Disrupted oxides	Large pores	Total porosity	Relative density
	(%)	(%)	(%)	(%)	(%)
1	0.905	0.580	0.950	2.435	97.565
2	0.415	0.435	0.205	1.055	98.945
3	0.265	0.065	0.185	0.515	99.485
4	0.240	0.240	0.460	0.940	99.060
5	1.050	0.450	3.380	4.880	95.120
6	1.235	0.045	0.880	2.160	97.840
7	0.835	0.110	0.540	1.485	98.515
8	0.690	0.025	0.365	1.080	98.920
9	0.480	0.015	0.190	0.685	99.315
10	0.555	0.025	0.195	0.775	99.225
11	0.430	0.020	0.185	0.635	99.365
12	0.425	0.015	0.170	0.610	99.390
13	0.450	0.015	0.175	0.640	99.360
14	0.360	0.025	0.125	0.510	99.490
15	0.435	0.030	0.165	0.630	99.370
16	0.335	0.015	0.110	0.460	99.540
17	0.245	0.025	0.080	0.350	99.650
18	0.225	0.010	0.100	0.335	99.665
19	0.225	0.035	0.060	0.320	99.680

The metallurgical pores are believed to form from entrapped gas, either processing gas (argon) or hydrogen. The disrupted oxides are irregular in shape (circularity < 0.8), and are formed either when the oxide films of neighbouring scan tracks trap gas or unmelted particles, or due to process related irregularities (e.g. incomplete coating or lack

of fusion). The large pores can be interpreted as large hydrogen pores, cracks due to residual stresses, keyhole pores, or process induced pores. Fig. 1 shows the cross section of sample 6 (a) and sample 14 (b). The different forms of porosity are indicated with arrows.

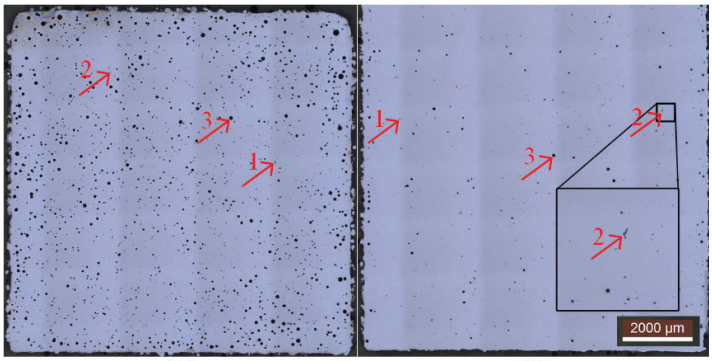

Fig. 1. Optical microscope image of test number 6 (a) and 19 (b). The red arrows indicate the different pore categories; 1) metallurgical pores, 2) disrupted oxides, 3) large pores. Inset in (b) is an enlarged view of a disrupted oxide.

Due to moisture and dissolved hydrogen in the powder particles, the melt is supersaturated with hydrogen [12]. In efforts to reduce the amount of hydrogen, the powder was pre-heated with the laser running at 50W on each layer. The initial tests showed a significant reduction in porosity because of the pre-heating [11]. It was suspected that keeping the substrate at an elevated temperature would further reduce the metallurgical porosity, which turned out not to be the case when comparing tests 1, 2 and 3 with test 7, 10, and 14 respectively. Although the occurrence of small metallurgical pores was not reduced, the amount of large pores and disrupted oxides were significantly reduced, leading to an overall increase in relative density when keeping the substrate heated during processing. The overall increase in relative density is consistent with findings of Weingarten et al. [12], but it cannot only be attributed to a reduction in hydrogen. Due to the elevated temperature in the substrate, the thermal gradient is lower, which will reduce the residual stresses, and thus the risk of cracking. Furthermore, increasing the substrate temperature reduces the required amount of energy input from the laser, allowing for a higher scan speed, which is shown to reduce the pore growth in the heat affected zone [12]. An added benefit with increasing the substrate temperature is that the scan speed can be increased, reducing the processing time of the material.

A common formulation to relate the different processing parameters to energy input is energy density (J/mm^3), as shown in Eq. (1) as the laser power over an estimate of the volume of the melt pool.

$$ED = P/vht \tag{1}$$

The additional energy input due to the heating of the substrate can be estimated from Eq. (2) [13], where Q is the required energy to melt a volume of material, ρ is the density of the material, c_p is the specific heat, and T_m and T_0 is the melting temperature and substrate temperature respectively. L_f is the latent heat of fusion.

$$Q = \rho c_p(T_m - T_0) + \rho L_f \tag{2}$$

We assume that the values for density, specific heat, melting temperature, and latent heat of fusion are 2.67 g/cm^3, 910 J/kg°C, 660 °C, and 510 kJ/kg respectively. Then, the difference in required energy to melt a volume of material when the substrate is at room temperature (25°C) compared to when the substrate is at 200°C is approximately 17%. Although this correction gives a more nuanced picture of the energy input to the material, the energy input according to Eq. (1) is in the order of 20 to 30 times the required energy to melt the feedstock according to Eq. (2). Effects such as thermal conductivity, absorptivity, and packing density of the powder are not included in the estimation model. Furthermore, the laser intensity distribution is assumed to be square, while in reality it is closer to a Gaussian distribution [12]. Using the layer thickness as a measure of the depth of the melt pool also imposes some problems. Firstly, the laser is required to melt a section of the preceding layer to secure proper bonding. Secondly, the melt pool will be moving in the path of the laser trajectory as an ellipsoidal shape, and not a square box [3]. The hatch spacing is used as a measure for melt pool width instead of the laser spot diameter to account for the overlapping of parallel scan tracks. Several other variables that will affect the effective energy input into the powder are also not considered; such as a different absorptivity in the molten material compared to the powder, evaporation of metal, and surface tension effects changing the geometry of the melt pool.

In an effort to illuminate the limitations of considering the melt pool as a box, consider the schematic in Fig. 2 comparing a rectangular melt pool cross section with a triangular melt pool cross section. The required power to form a melt pool of a certain volume per time unit can be expressed as:

$$QV = \eta P \tag{3}$$

Where Q is the required energy to melt a unit volume of material (Eq. (2)), and V is the volume of the melt pool in terms of scan speed, $V = \frac{1}{2} d t_p v$, where t_p is the depth of penetration. P is the laser power, and η is the absorptivity of the laser in the powder. By combining Eqs. (2) and (3) the depth of penetration can be calculated in terms of material constants, laser parameters, and scan velocity:

$$t_p = \frac{\eta P}{\frac{1}{2} d v \rho (c_p(T_m - T_0) + \rho L_f)} \tag{4}$$

The accuracy of the estimate from Eq. (4) can easily be determined experimentally. In this study, this has been done by comparing the calculated depths of penetration with experimentally quantified depths of penetration for single-track laser powder bed fusion published by Aboulkhair et al. [14]. The average error is 9.6%.

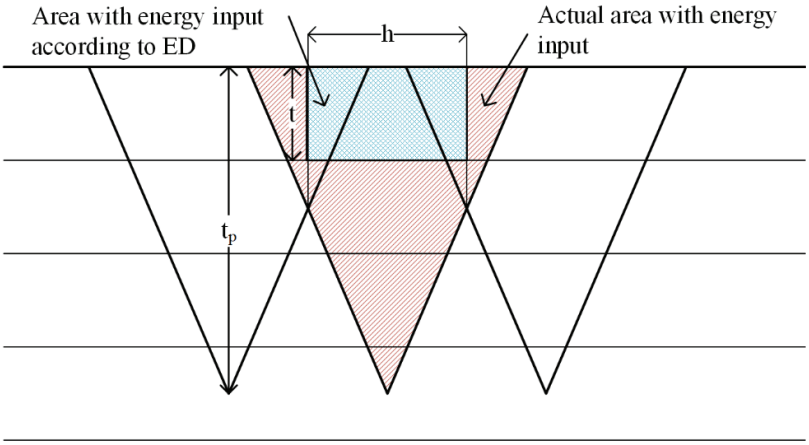

Fig. 2. Schematic of three overlapping laser tracks in a LPBF process.

Since the depth of penetration is a function of the laser power, laser spot diameter, and the laser scan speed, presenting the energy input in terms of *ED* seems disadvantageous. Instead of being concerned with the volumetric energy input, the process can rather be designed to have a depth of penetration sufficient to secure full bonding between the powder layer and the previous layer, and assuring the hatch spacing is wide enough to make sure the neighbouring tracks overlap sufficiently.

4 Conclusions

This study has shown that a relative density of AlSi10Mg processed by laser powder bed fusion of above 99.6% can be achieved by proper selection of process parameters. Initial investigation revealed that pre-heating the powder at each layer with 50W laser power reduces the occurrence of metallurgical pores, likely due to a reduction of moisture (hydrogen) in the powder feedstock. Increasing the substrate temperature from room temperature to 200°C reduced the occurrence of disrupted oxides and large pores, but did not significantly reduce the occurrence of metallurgical pores. An increase in relative density, accompanied by an increased build rate, was observed when the substrate was held at 200°C.

The authors propose that hatch spacing and layer thickness should be chosen based on an estimated laser penetration depth instead of the commonly used ‘energy density’. The depth of penetration is a function of scan velocity, laser properties, and material properties, and can be calculated within reasonable accuracy when the laser properties and material properties are known.

Acknowledgements. The authors acknowledge funding from the Research Council of Norway (grant no. 248243/MKRAM project). The authors thank Vegard Brøtan, Johan

Fahlström and Eirik Morset (SINTEF Raufoss Manufacturing) for valuable contribution in design and installation of the heating system in the LPBF machine.

References

1. E.O. Olakanmi, R.F. Cochrane, K.W. Dalgarno, A review on selective laser sintering/melting (SLS/SLM) of aluminium alloy powders: Processing, microstructure, and properties, Progress in Materials Science 74 (2015) 401-477.
2. L. Thijs, K. Kempen, J.-P. Kruth, J. Van Humbeeck, Fine-structured aluminium products with controllable texture by selective laser melting of pre-alloyed AlSi10Mg powder, Acta Materialia 61(5) (2013) 1809-1819.
3. W. King, A. Anderson, R. Ferencz, N. Hodge, C. Kamath, S. Khairallah, A. Rubenchik, Laser powder bed fusion additive manufacturing of metals; physics, computational, and materials challenges, Applied Physics Reviews 2(4) (2015) 041304.
4. A. Wu, D. Brown, M. Kumar, G. Gallegos, W. King, An Experimental Investigation into Additive Manufacturing-Induced Residual Stresses in 316L Stainless Steel, Metallurgical and Materials Transactions A 45(13) (2014) 6260-6270.
5. N.T. Aboulkhair, N.M. Everitt, I. Ashcroft, C. Tuck, Reducing porosity in AlSi10Mg parts processed by selective laser melting, Additive Manufacturing 1-4 (2014) 77-86.
6. W. Li, S. Li, J. Liu, A. Zhang, Y. Zhou, Q. Wei, C. Yan, Y. Shi, Effect of heat treatment on AlSi10Mg alloy fabricated by selective laser melting: Microstructure evolution, mechanical properties and fracture mechanism, Materials Science and Engineering: A 663 (2016) 116-125.
7. Y. Liu, Y. Yang, S. Mai, D. Wang, C. Song, Investigation into spatter behavior during selective laser melting of AISI 316L stainless steel powder, Materials & Design 87 (2015) 797-806.
8. M. Simonelli, C. Tuck, N.T. Aboulkhair, I. Maskery, I. Ashcroft, R.D. Wildman, R. Hague, A Study on the Laser Spatter and the Oxidation Reactions During Selective Laser Melting of 316L Stainless Steel, Al-Si10-Mg, and Ti-6Al-4V, Metallurgical and Materials Transactions A 46(9) (2015) 3842-3851.
9. E. Malekipour, H. El-Mounayri, Common defects and contributing parameters in powder bed fusion AM process and their classification for online monitoring and control: a review, The International Journal of Advanced Manufacturing Technology 95(1) (2018) 527-550.
10. G. Casalino, S.L. Campanelli, N. Contuzzi, A.D. Ludovico, Experimental investigation and statistical optimisation of the selective laser melting process of a maraging steel, Optics & Laser Technology 65 (2015) 151-158.
11. A. Djuraev, H.J. Roven, O. Reiso, T. Furu, Porosity Reduction and Characterization of Aluminium Components Produced by Additive Manufacturing, NTNU, 2017.
12. C. Weingarten, D. Buchbinder, N. Pirch, W. Meiners, K. Wissenbach, R. Poprawe, Formation and reduction of hydrogen porosity during selective laser melting of AlSi10Mg, Journal of Materials Processing Technology 221 (2015) 112-120.
13. I. Yadroitsev, P. Krakhmalev, I. Yadroitsava, S. Johansson, I. Smurov, Energy input effect on morphology and microstructure of selective laser melting single track from metallic powder, Journal of Materials Processing Technology 213(4) (2013) 606-613.
14. N.T. Aboulkhair, I. Maskery, C. Tuck, I. Ashcroft, N.M. Everitt, On the formation of AlSi10Mg single tracks and layers in selective laser melting: Microstructure and nano-mechanical properties, Journal of Materials Processing Technology 230 (2016) 88-98.